Precision microwave spectroscopy in a Ku-band waveguide: the case study of the 12.2 GHz line of methanol

Simon Collignon[a,b], Brian Hays[a,c], Dimitri Lederer[b], Clément Lauzin[a]

[a] *Institute of Condensed Matter and Nanosciences, UClouvain, Louvain-la-Neuve, 1348, Belgium*
[b] *Institute of Information and Communication Technologies, Electronics and Applied Mathematics, UCLouvain, Louvain-la-Neuve, 1348, Belgium*
[c] *Univ. Lille, CNRS, UMR 8523 - PhLAM - Physique des Lasers Atomes et Molécules, Lille, 59000, France*

Abstract

Accurate rest frequencies of torsion-rotation transitions of methanol in the centimeter wave are critical to challenge the standard model through probing hypothetical variation of fundamental constants over space and time. Even though microwave Fourier transform (FTMW) spectroscopy is a very mature technique, it fails to provide uncertainties below the kHz level and the characterization of these uncertainties remains scarce. Here, we employ a new FTMW spectrometer to measure and analyze the free induction decay (FID) signal of the 12.2 GHz torsion-rotation transition of methanol in the time domain. We discuss the systematic effects that induce a shift on the line center and quantify the associated corrections and uncertainties that pertain to the frequency estimate. The transition frequency was determined to be $12,178,596,106 \pm (12)_{\mathrm{stat}} \pm (243)_{\mathrm{sys}}$ Hz. This work not only provides a reference to further constrain the limit on hypothetical variation of the proton-to-electron mass ratio, but also compiles the many systematic effects that must be accounted for in general to accurately quantify the uncertainty of the frequency estimated from FID signals.

Keywords: FTMW, FID, Precision

1. Introduction

CH_3OH is the second most abundant volatile organic compound in our atmosphere [1] and displays some of the most brightest masers observed in the interstellar medium (ISM). The 12.2 GHz [2] and 6.7 GHz [3] lines are two of the most intense and widespread class II masers observed in the ISM [4, 5]. As population inversion is achieved through radiative pumping by nearby infrared sources, these masers can serve as tracers of star-forming regions. In addition, the polarization of these masers provide information on the magnetic field arising nearby these young stellar objects [6]. Molecules with internal rotors play an important role in interstellar chemistry [7]. In methanol, the methyl group within the molecule exhibits hindered rotation with respect to the hydroxy frame. This large amplitude motion was also shown to enhance the sensitivity of some transitions with respect to the hypothetical variation of the proton-to-electron mass ratio $\mu = m_p/m_e$ [8, 9, 10]. The 12.2 GHz transition is one of the most sensitive line to μ-variations. This line, with other methanol transitions, were measured in absorption towards the quasar PKS-1830-211 at a redshift $z \approx 0.89$ to derive the most stringent constraint on the μ-variation [11, 12, 13, 14, 15]. Comprehensive reviews on the use of methanol and other molecules to constrain fundamental constants are provided in Ref. [16] and Ref. [17].

Probing μ-variations requires accurate rest frequencies for the methanol transitions involved. These were first made available by Lee et al. in 1973 [18] and were updated in 2004 by Müller et al. [4]. These works quote the rest frequency of the 12.2 GHz methanol line based on experimental measurements performed with two types of spectrometers. First, this transition was studied with a beam-maser experiment described in Ref. [19]. Then, it has been re-measured numerous times with Fourier-transform microwave (FTMW) spectrometers of the Balle-Flygare type [20, 21, 22]. The 1σ frequency uncertainties reported in these works at best reach the $\sim$ 1 kHz level, that is a relative frequency uncertainty of $\Delta\nu/\nu = 10^{-7}$. Jansen et al. conceptualized Rabi- and Ramsey-type instruments, employing a Stark-deflected beam of methanol [23]. Such experiments are routinely used in microwave frequency standards to reach $\delta\nu\ /\nu < 10^{-12}$ [24]. However, the hyperfine levels involved in the torsion-rotation transitions in methanol makes it challenging to achieve state selectivity. We propose in this work to use a FTMW spectrometer coupled to a room-temperature waveguide cell to study the rest frequency of the 12.2 GHz transition. Resonant frequency and other line parameters are estimated through the fit of the time-domain, coherent molecular emission signal called the free induction decay (FID), sometimes referred to as the free optical precession. FID signals have been studied for a long time to determine the broadening parameters of polar molecules in the gas phase [25, 26, 27]. In a recent experiment, time-domain fitting of the FID was used to reach a relative uncertainty of 0.72 Hz between the line centers of a same transition, measured for both enantiomers of 1,2-propanediol [28]. Reducing such uncertainty is critical to observe significant frequency difference between enantiomers and probe a possible parity violation [29]. Such endeavors, currently limited by instrumental methods, further motivate the need for accurate

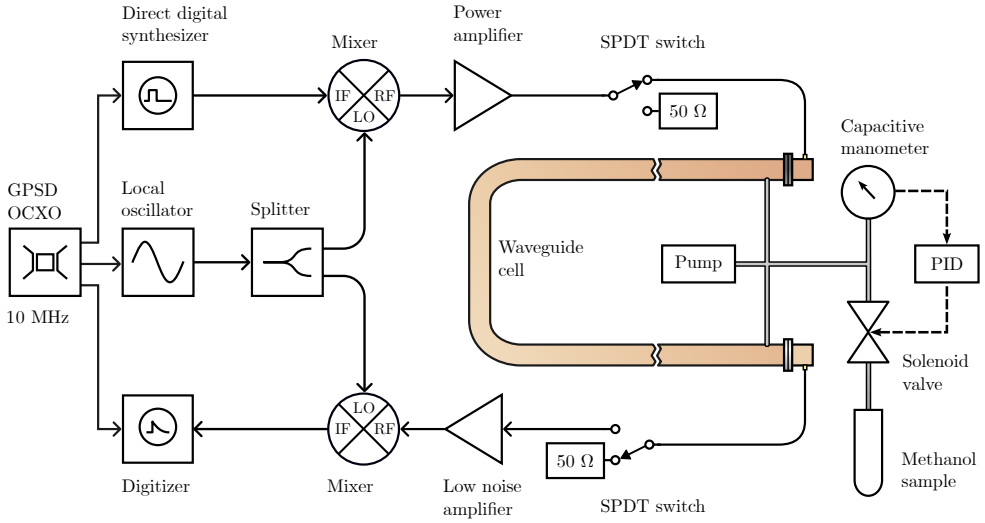

Figure 1: Block diagram of the experimental setup. See main text for details.

microwave techniques to tackle these fundamental questions in physics and chemistry.

Other fields have considered the problem of frequency estimation from FID signals. In nuclear magnetic resonance, magnetometers indirectly measure the external magnetic field B_0 by estimating the resonant frequency of the FID, that is the Larmor frequency ν_L, linked through the relation $\nu_L = \gamma B_0/(2\pi)$, where γ is the gyromagnetic ratio. Quantification of the frequency uncertainty is then an important part of the instrumental characterization as it directly relates to the sensitivity of these devices to external magnetic fields [30, 31, 32]. We propose here a similar analysis for the case of microwave FIDs observed from rotational transitions.

Finally, a 10^4 gap in fractional uncertainty exists between the microwave spectroscopy techniques and state-of-the-art experiments in the optical domain that now reach $\Delta\nu/\nu = 10^{-11}$ [33]. The latter then become competitive for the accurate measurements of pure rotational transitions in the ground vibrational state using the combination differences technique and the construction of molecular energy levels network [34]. Such indirect measurement schemes would benefit from accurate microwave rest frequencies for validation and benchmarking purposes.

In the remainder of this manuscript, we first provide in Sec. 2 a description of the experimental setup, consisting of a newly built FTMW spectrometer coupled to a Ku-band rectangular waveguide cell. The measurements of the 12.2 GHz methanol transition are presented in Sec. 3. In that section, we first derive the FID model used to fit our experimental data. Then, all systematic effects on the line center frequency are presented. These effects are finally summarized in an error budget containing all the corrections and uncertainties to apply on the estimated transition frequency of the 12.2 GHz methanol line. We also provide a comparison between our work and the already published rest frequencies of that particular transition. In Sec. 4, we present perspectives where the uncertainty around the frequency estimate of microwave FIDs could be reduced by up to two orders of magnitude, down to its fundamental limit. Concluding remarks are provided in Sec. 5.

2. Experimental

The block diagram in Figure 1 presents a simplified version of the new Ku-band, Fourier-transform microwave (FTMW) spectrometer, set up to probe polar molecules located inside a Ku-band waveguide cell. In the present work, the spectrometer is configured to perform narrowband excitation around the 12.2 GHz torsion-rotation transition in methanol. To this end, based on Refs. [35, 36], a direct digital synthesizer (DDS, Analog Devices, AD9914) first generates a 175 ns chirped pulse from 196.35 MHz to 196.45 MHz in the intermediate frequencies. The microwave pulse is then brought into the Ku-band by a RF mixer (Analog Devices, HMC8191, eval. board). This mixer is driven by a 12.375 GHz carrier signal produced by the local oscillator (Anritsu, 68067C). Both sidebands of the upconverted chirped pulse are amplified by a power amplifier (Techniwave, TWAMP618GHz) to reach an estimated final power of up to $\sim$ 17 dBm before enterging the waveguide cell through the transmitting single pole, double-throw (SPDT) switch (Analog Devices, ADRF5144 eval. board). The output power of the spectrometer is set to reach effective $\pi/2$-pulse conditions by a manual tuning of the amplitude of the DDS output to about 8% of its voltage vertical range. The maximum amplitude E_0 of the external electric field inside the waveguide is estimated to be $\sim$ 1 kV/m. In this probing scheme, the lower sideband is Fourier-transform limited (i.e., displays a sinc profile in the frequency domain) and encloses the resonant frequency of the transition of interest. The chirped pulse travels through the 2.6 m waveguide, polarizes the molecules, exits the cell and finally dissipates in the 50 Ω load of the second SPDT switch, placed at the frontend of the RF detection chain of the instrument. Shortly after, both RF switches are toggled to (i) isolate the noisy power amplifier from the waveguide cell and (ii) direct the free induction decay signal in the RF detection chain. The weak molecular signal is amplified, downconverted back

to intermediate frequencies with the same carrier signal as for the excitation, and finally digitized with a fast PCIe digitizer (SP devices, ADQ32). The FID is acquired over $\sim$ 35 μs at a sampling rate of 2.5 GSa/s. This overall excitation-detection sequence is repeated at a 25 kHz rate. All generated FIDs are captured by the acquisition card, thanks to its low trigger rearm time of 20 ns and its ability to acquire new data while transferring past waveforms onto the host computer memory. The acquired molecular signals are co-added on the fly on both the acquisition card and the host computer to improve signal-to-noise ratio (e.g., 10^8 FIDs are routinely co-added in about 1.2 hours). The high data-throughput capabilities of the spectrometer plays a crucial role in the current project where experiments need to be repeated a large number of times to achieve the best SNR possible. Timing and triggering signals are generated by a digital delay generator (BNC, Model 577). All RF oscillators (delay generator included) running in the spectrometer are synchronized on the same 10 MHz, GPS-disciplined oven-controlled Quartz oscillator (GPSD-OCXO, Jackson Labs, Fury). It provides a frequency stability $\Delta\nu/\nu$ better than 10^{-11} for integration times greater than 0.1 s.

The FTMW spectrometer connects to both ends of the U-shaped, Ku-band waveguide cell. Two vacuum ports are symmetrically placed near the RF ports. Pumping and sample injection are performed simultaneously through both vacuum ports to minimize the pressure gradient that would arise otherwise in a flow cell arrangement. The liquid methanol sample (VWR chemicals, > 99.9% purity) is held at room temperature inside a glass holder. The vapor pressure above the liquid methanol sample is injected into the waveguide through a solenoid valve (Bürkert, type 2871). The 0.05 mm nominal diameter of the valve limits the maximum methanol pressure to $\sim$ 10 Pa inside the waveguide cell. The sample pressure is measured with a temperature controlled, absolute Baratron capacitance manometer (MKS, 627H), rated for a 0.12% reading accuracy between 5 Pa and 5×10^{-3} Pa. Pressure inside the cell is stabilized by a PID controller that runs on the instrument computer. Based on Ref. [37], the PID controller reads pressure and throttles the injection solenoid valve through an arduino R4 minima at a $\sim$ 600 Hz repetition rate. The control loop achieves a pressure stability of $\sim$ 2 mPa (one standard deviation) and covers a pressure range from 0.05 Pa to 1 Pa. The temperature is monitored with a resistance temperature sensor fixed on the outside of the waveguide (PT100 with a MAX31865 amplifier in 3-wire configuration, Adafruit, ±0.5 K accuracy). Both the spectrometer and the injection system are fully automated through a custom Python, Pyside6 software. It allows the instrument to run 24/7 and perform automated parametric studies by incrementing one of the experiment parameters, such as the methanol pressure inside the waveguide or the amplitude of the microwave pulse produced by the DDS.

3. Results

This work focuses on the accurate line center determination of the $J'_{K'}\Gamma' \leftarrow J''_{K''}\Gamma'' = 2_0\ E \leftarrow 3_{-1}\ E$ transition in methanol, where J and K are the rotational quantum numbers and Γ is the symmetry species. These torsion-rotation states possess a rich hyperfine structure, due to nuclear spin-spin, spin-rotation and spin-torsion couplings [38, 39]. It typically extends over 25 kHz. Spectral features measured with the experimental setup detailed above display a minimum full width at half maximum (FWHM) of $\sim$ 30 kHz. The underlying hyperfine lines of the $2_0\ E \leftarrow 3_{-1}\ E$ transition are therefore not resolved. At thermodynamical equilibrium, the line center coincides with the centroid ν_0 of the unresolved hyperfine multiplet, defined as [33]:

$$\nu_0 = \frac{\sum_i S_i \nu_i}{\sum_i S_i} \tag{1}$$

The centroid is the average of the hyperfine line centers ν_i weighted by the relative FID amplitudes S_i associated to the hyperfine transitions within the multiplet. The accuracy of the method used in this work to estimate the centroid ν_0 from the convolved hyperfine mutliplet is numerically investigated in Sec. 3.2.

3.1. Lineshape

A room-temperature waveguide cell presents several advantages compared to Balle-Flygare experiments that operate with pulsed molecular beams. First, the methanol sample is at thermodynamical equilibrium with well defined pressure and temperature conditions. Then, both the external and molecular radiation fields are confined to the well-defined TE_{10} mode of the Ku-band rectangular waveguide. The FID signal in such well-behaved experimental conditions can be accurately described by an analytical model [40, 41]. In this work, the nonlinear least-squares (NLS) fit of the FID model onto the experimental data is employed to retrieve the centroid ν_0 of the $2_0\ E \leftarrow 3_{-1}\ E$ methanol line. A simple, general expression general of the FID model is written as follows:

$$f(t) = A s(t) \cos\left(2\pi\nu t\ + \phi\right) \tag{2}$$

where $f(t)$ has an amplitude A and oscillates at a the resonant frequency ν with a phase ϕ. The function $s(t)$ is the decaying envelope of the FID, caused by the relaxation of the induced population difference and coherence between the levels involved in the transition. The decaying envelope chosen in this work is set by the quadratic speed-dependent Voigt (qSDV) profile, first introduced by Rohart et al. [26, 42]. In the time domain, the envelope $s(t)$ of the qSDV model is written as follows [41, 43]:

$$s(t) = \frac{W(t)}{(1+\Gamma_2 t)^{3/2}} \exp\left[-\left(\Gamma_0 - \frac{3}{2}\Gamma_2\right)t\right] \exp\left[-\frac{(k\mathrm{v}_0 t)^2}{4(1+\Gamma_2 t)}\right] \tag{3}$$

The Doppler term involves the wavenumber of the transition k and the most probable speed $\mathrm{v}_0 = \sqrt{2k_B T/m}$ of molecules of mass m. The pressure broadening rate Γ_0 is related to the pressure broadening coefficient γ by the relation $\Gamma_0 = 2\pi\gamma\ \times p$ where p is the pressure of the emitting molecules [27]. The parameter $\Gamma_2 > 0$ captures the quadratic dependence of the overall pressure broadening rate with respect to the speed of the emitters [26]. This relaxation model was chosen over a typical Voigt model as a clear departure from this profile is observed at

later times in the experimental FIDs [42]. Also, fitting the Voigt profile to the experimental FIDs, a dependence of the pressure broadening γ to the delay t_0 is observed, with $\partial\gamma/\partial t_0 < 0$. This effect suggests the presence of speed-dependence in microwave FID experiments [26, 44]. Finally, we also selected the qSDV model because it exhibits the smallest fitting residuals among all the tested line profiles (see Sec. A of the supplementary material).

Additionally, the function $W(t)$ in Eq. 4 models the collisions of the emitters with the broad walls of the waveguide. The broadening by wall collisions $W(t)$ is written as [40]:

$$W(t) = \mathrm{erf}\left(\frac{b}{\mathrm{v}_0 t}\right) + \frac{t}{b}\frac{\mathrm{v}_0}{\sqrt{\pi}}\left[\exp\left\{-\left(\frac{b}{\mathrm{v}_0 t}\right)^2\right\} - 1\right] \qquad (4)$$

where b is the distance that separates the inner broad walls of the Ku-band waveguide and evaluates to 7.9 mm. Relaxation caused by microwave field inhomogeneities and collisions with the short walls [40] are estimated to be negligible and are not considered in this work.

All the line parameters are estimated by the NLS fit of the qSDV model to the experimental FID signals, over a time window $[t_0, t_f]$. The lower bound t_0 is the delay between the end of the excitation pulse and the start of the time window used for the fit. We set $t_0 = 1.42\,\mu$s since data points acquired before that time are corrupted by instrumental transients, mainly caused by the finite time response of the RF switches, and are therefore discarded. This delay must be taken into account when the argument of the exponentially decaying envelope is non-linear with respect to time [45]. The time window, $t_f - t_0$, is typically 30 μs. Regarding the fitting routine, we used the Levenberg-Marquardt algorithm [46] implemented in the `curve_fit` function from SciPy [47]. The qSDV parameters left floating for optimization are the amplitude A, the frequency ν and a constant phase ϕ of the FID, along with the broadening and speed-dependent rates Γ_0 and Γ_2. The temperature, pressure and delay t_0 are fixed to their measured, experimental values.

Active stabilization of the methanol pressure inside the waveguide works over a pressure range that covers one order of magnitude, from ~0.08 Pa to ~0.8 Pa. As an example, two experimental FIDs measured at these two pressure limits are shown in the top and middle panels of Fig. 2, respectively. Zoom insets show the qSDV model fit to the experimental data points. For both FIDs, the three components of the relaxation envelope $s(t)$ from Eq. 3 are represented, namely the Doppler, wall and self broadening relaxation components. At the lowest pressure limit, all these relaxation mechanisms contribute almost equally to the envelope $s(t)$. For the highest pressure limit, self broadening is dominating the total relaxation function. One can see that two distinct relaxation regimes were explored within the working pressure range. The residuals of the fitted FIDs are shown in the bottom panel of Fig. 2, along with a reference noise trace acquired in an empty waveguide, with the same experimental conditions otherwise. A transient decaying feature is observed in both residuals but not in the reference signal. These are attributed to a nearby transition polarized by the side lobes of the Fourier-transform limited excitation pulse. To

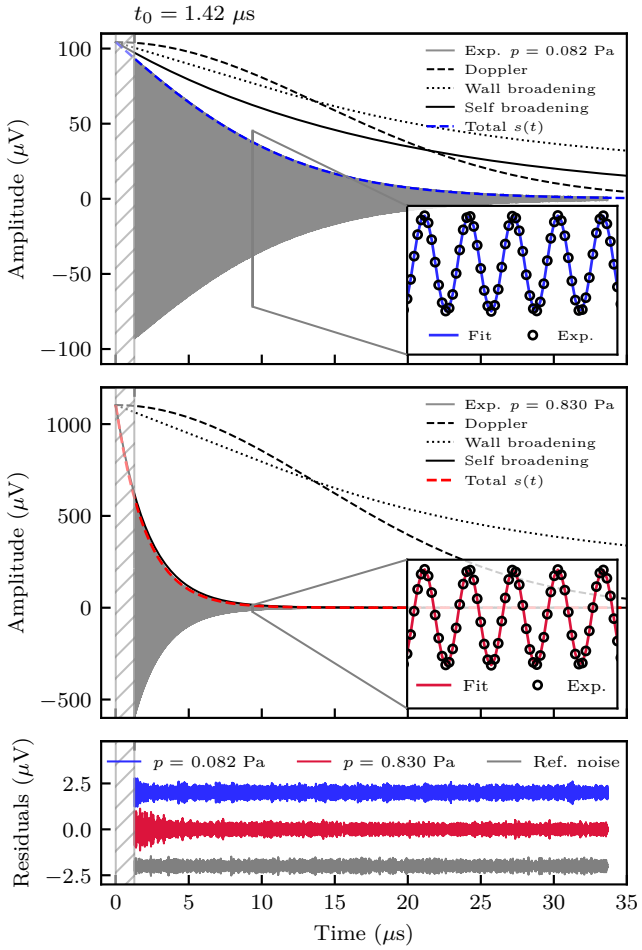

Figure 2: Fit and relaxation analysis of the experimental $2_0\ E \leftarrow 3_{-1}\ E$ FID measured at 0.082 Pa (top panel) and 0.83 Pa (middle panel). The insets highlight the quality of the fit for both pressure regimes using the qSDV model. Decaying envelopes are broken down between the relaxation contributions extracted from the fit. Residuals of both experiments are displayed and compared to a reference noise signal (bottom panel). Hatched region represents the delay t_0 between the end of the MW pulse and the start of the FID truncation window.

further discuss the validity of the FID model, the Fourier transform of all traces of Fig. 2 is shown in Fig. 3. The real part of these Fourier-transformed signals is displayed after rephasing to only account for the absorptive part (i.e., real part) of the spectrum and suppress the erroneous lineshape pedestal that comes with the dispersive part (i.e., imaginary part). The real part of the rephased spectrum $\hat{f}[k]$ is written as:

$$\hat{f}[k] = \Re\{\exp\left[-i(\tilde{\phi} + \tilde{\nu} t_0)\right] \mathrm{FFT}\,(f[n])\,\} \qquad (5)$$

where n and k are discrete time and frequency indices. i is the imaginary number. $f[n]$ is the model $f(t)$ of Eq. 2 sampled at times $t = n\tau_s$ with a sampling frequency of $\nu_S = 1/\tau_S = 2.5$ GHz. Rephasing is performed using the initial phase of the FID at the start of the truncation window, recovered from the fit of the qSDV model and denoted $\tilde{\phi} + \tilde{\nu}_0 t_0$. Tilted parameters are estimates obtained by NLS optimization. The same treatment was applied to residuals, shown in the bottom panel of Fig. 3. There, features are visible in both residuals, centered on

the centroid of the transition and more pronounced for the lowest pressure experiment. Although difficult to distinguish from other effects that may cause these residual features, one plausible explanation is the underlying hyperfine transitions in the convolved multiplet, displayed as a stem plot in the top panel of Fig. 3. The positions and intensities of these transitions were calculated by Lankhaar et al. and taken from their supplementary material in Ref. [39]. The impact of these hyperfine lines on the quality of the fit, along with other systematic effects, are discussed in the following sub-sections.

3.2. *Hyperfine transitions*

The qSDV model defined above describes the profile of an isolated line. Fitting a single-line profile to a convolved multiplet introduces a systematic error on the centroid frequency estimated from the fit. To evaluate this systematic error, we performed a numerical experiment in which we fitted the isolated qSDV model to a sum of 22 synthetic FIDs. These FIDs

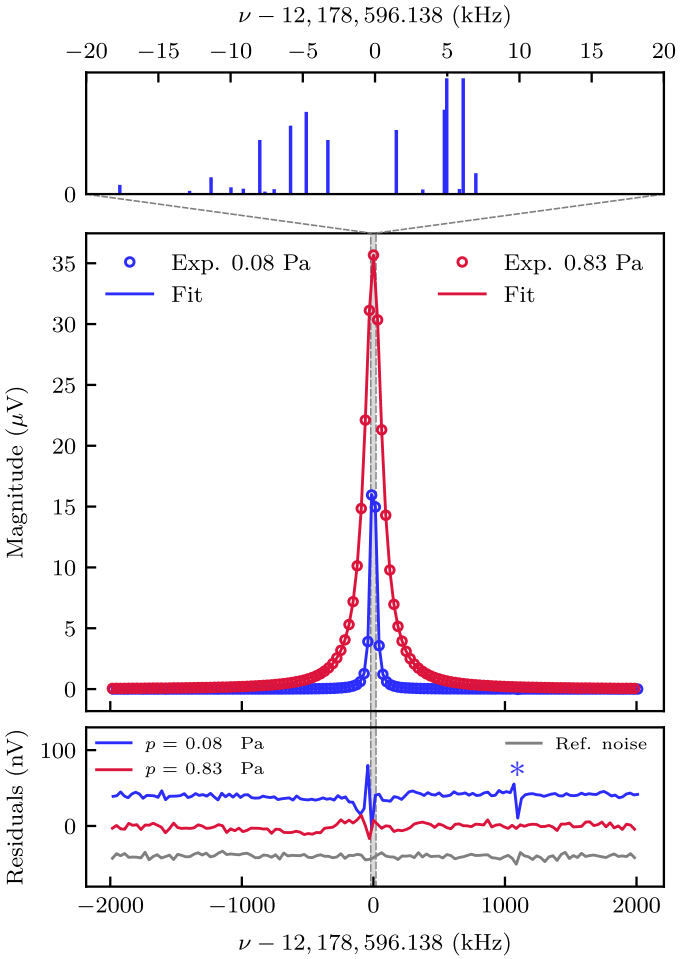

Figure 3: Rephased Fourier transform of the FID signals with the fit of the corresponding qSDV models (middle panel) and the residuals displayed in Fig. 2 (bottom panel). The stick plot (top panel) indicates the positions and relative intensities of the hyperfine transitions calculated in Ref. [39]. The ~ 40 kHz frequency window in the top panel is represented as a gray, dashed strip across the middle and bottom panels. The blue asterisk symbol indicates the location of a random electrical spurious.

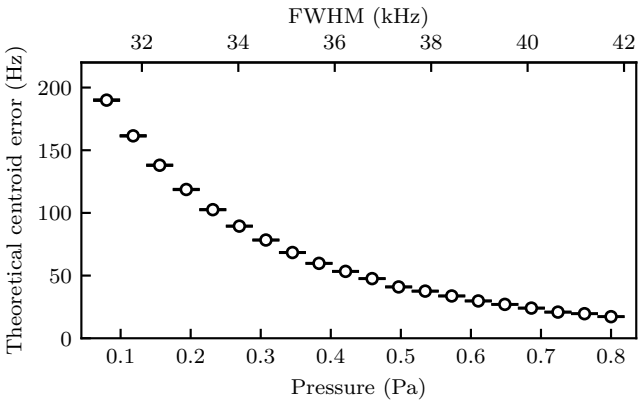

Figure 4: Numerical evaluation of the systematic error on the estimated centroid frequency of the $2_0\ E \leftarrow 3_{-1}\ E$ of methanol. It arises from the fit of the isolated qSDV line profile to the hyperfine multiplet of this transition. Relative amplitudes and frequencies of the hyperfine components within the multiplet were set to the theoretical values calculted by Lankhaar et al. [39] and are shown in the top panel of Fig. 3.

have the same line parameters, except for their amplitudes and frequencies which are set by the hyperfine transitions displayed in the top panel of Fig. 3, as calculated in Ref. [39]. In Fig. 4, the systematic error on the estimated centroid resulting from this simulation is shown over the typical pressure range covered in our experiments. The error increases non-linearly as the pressure decreases and reaches 211 Hz at 0.08 Pa. The convolved multiplet has a smaller FWHM at low pressure and small asymmetries on the line profile are better resolved. Since these asymmetries are not captured by the isolated line shape, they induce a systematic shift during the fitting routine. In contrast, working at higher pressure mitigates this systematic effect and the error on the estimated centroid tends towards zero [33].

3.3. *Pressure shift*

It is well known that line parameters, such as line center and broadening, depend on pressure. This dependence is evaluated by measuring FID signals at seven different pressure points, ramping up over the usable range of the instrument, from 0.08 Pa to 0.8 Pa. One FID measurement at a given pressure takes 35 minutes to complete, after which a total of 20 million phase-stable FIDs are acquired and averaged together. These pressure ramp measurements were repeated back to back 34 times over the course of a four-day measurement campaign. It is worth noting that looping over these pressure ramps that many times was reasonably made possible thanks to the automated experimental processes described in Sec. 2. The objective of these repetitions is two-fold. First, to check the good reproducibility of these pressure-ramp experiments over a few days. Second, and more importantly, to evaluate the statistical uncertainty around the estimated centroid, defined as the standard deviation σ_ν^{stat}. The seven estimated centroids, averaged over the 34 individual pressure ramps, are displayed in the top panel of Fig. 5. The vertical and horizontal error bars are the standard deviations with respect to frequency σ_ν^{stat} and pressure σ_p^{stat}, respectively. The zoomed inset in this panel focuses on the es-

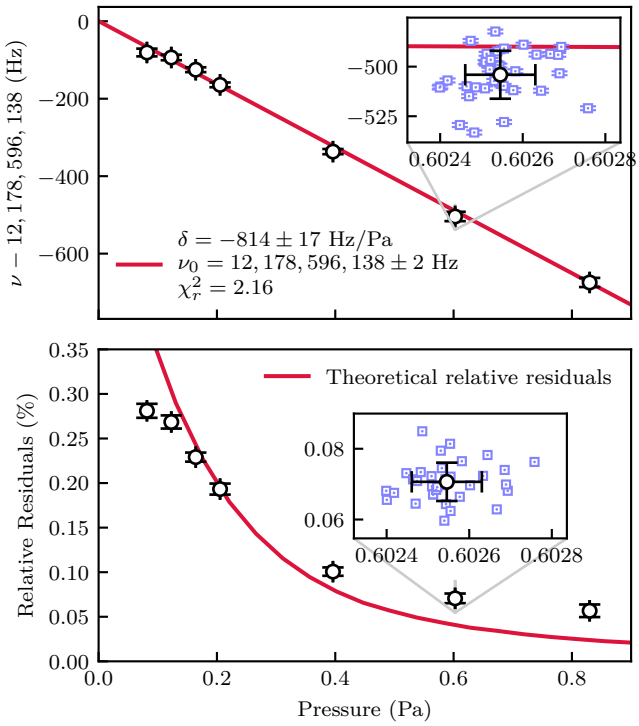

Figure 5: Top panel: estimated centroids (black circles), weighted linear least-squares fit (red trace). Inset: zoom on the estimated centroid at $p \approx 0.6$ Pa (black circle) resulting from the average taken over all frequency estimates (blue dotted boxes) retrieved from the fit of 34 distinct FID measurements. Error bars around the estimated centroids are the standard deviations σ_ν^{stat} (vertical) and σ_p^{stat} (horizontal). The error bars around the fit frequency estimates are σ_ν^{fit}. Bottom panel: averaged relative residuals corresponding to the peak magnitude FFT of the FID divided by the peak magnitude FFT of the residuals, expressed in % (black circles). In total, the data shown in this figure result from the fit of 238 FID measurements, each averaged 20 million times.

timated centroid for the $p = 0.6$ Pa pressure setting and reveals the 34 individual frequency estimates (dotted blue boxes) that were used in the calculation of the average and standard deviation. The error bars on these estimates are the standard uncertainties σ_ν^{fit} computed from the covariance matrix of the NLS fitting routine. The one order of magnitude discrepancy between σ_ν^{stat} and the average fit uncertainty $\left\langle \sigma_\nu^{\text{fit}} \right\rangle$ is further discussed in Sec. 4. To recover the non-shifted centroid frequency ν_0, we perform a weighted, linear least-squares fit of the model $\nu(p) = \delta p + \nu_0$ to the seven estimated centroids. Through this fitting procedure, a negative pressure shift $\delta = -814 \pm 17$ Hz/Pa is determined, along with the centroid frequency at zero pressure $\nu_0 = 12,178,596,138 \pm 2$ Hz.

The bottom panel in Fig. 5 displays the average relative residuals and their standard deviations over the repeated pressure-ramp experiments. The relative residuals are defined in the spectral domain as the peak magnitude FFT of the time-domain residuals against the peak magnitude FFT of the measured FID. The relative residuals are maximum at low pressure and culminate at 0.3 %. Overall, such low relative residuals demonstrate the excellent agreement between the qSDV model and the 238 FID measurements fitted in total. Furthermore, the upward trend at low pressure is well reproduced by the theoretical relative residuals computed from the fit of the qSDV model isolated line shape to the numerical convolved hyperfine multiplet, described in Sec. 3.2. While other effects may contribute, it might suggest that relative residuals are limited at low pressure by the presence of the underlying hyperfine transitions.

3.4. Rabi shift

One key advantage of microwave coherent emission techniques over absorption spectroscopy is the background free detection of molecular signals. The interaction between the external field and the molecules is switched off prior observation such that the FID signal is not affected by power broadening or AC Stark shift. However, a line-shift that depends on the external field conditions may still be observed. It more generally depends on the Rabi flip angle and is referred to as the Rabi line-shift in the remainder of this work. Considering the $2_0\ E \leftarrow 3_{-1}\ E$ transition, the underlying hyperfine lines are assumed to be a set of uncoupled two-level systems polarized by a short and resonant MW pulse. The relative FID amplitude S_i

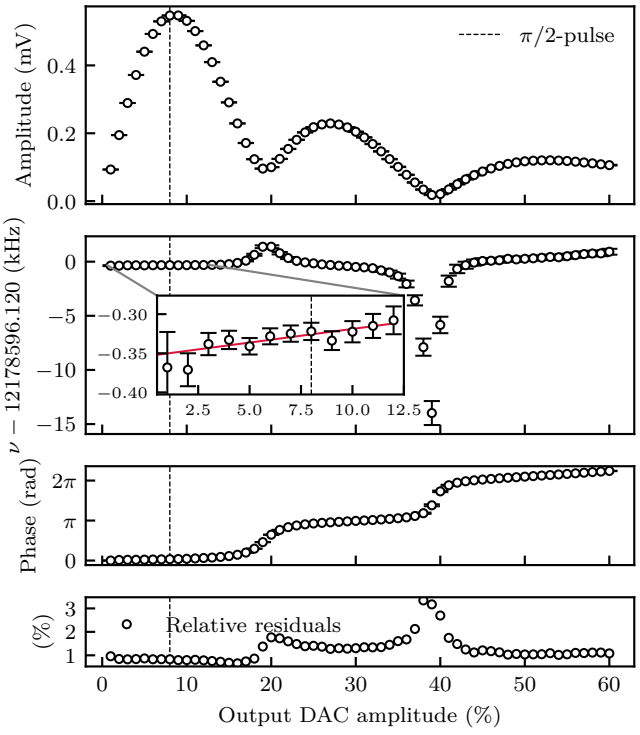

Figure 6: Fit parameters of the $2_0\ E \leftarrow 3_{-1}\ E$ FID as a function of the output DAC amplitude of the DDS. Other experimental conditions were held constant with a methanol sample pressure of 0.396 ± 0.002 Pa, a temperature of 299.3 ± 0.2 K and a MW pulse duration $\tau = 175$ ns. (a) Fit amplitude of the FID that undergoes Rabi oscillations. (b) Fit centroid frequency, the inset displays the linear fit of an hypothetical polarization line shift. (c) Relative phase of the fit FIDs. (d) Relative residuals of the fit FIDs. Vertical dashed line indicates the working point used for all other experiments presented in this work, where near optimal $\pi/2$-pulse polarization is achieved by setting up the output DAC amplitude of the DDS to 8%.

of the i-th hyperfine transition then follows [48]

$$S_i \propto \mu_i \left| J_1 \left(\Omega_{R,i} \tau \right) \right| \quad \text{with} \quad \Omega_{R,i} = \frac{\mu_i E_0}{\hbar} \tag{6}$$

where J_1 is the Bessel function of the first kind, E_0 is the amplitude of the external electric field at the center of the waveguide in the case of the TE_{10} mode and τ is the pulse duration. These hyperfine amplitudes oscillate at different Rabi frequencies $\Omega_{R,i}$ as these are directly proportional to the hyperfine transition dipole moment μ_i. Rabi oscillations following a J_1 Bessel function rather than a sine function arises from the fact that both the external and molecular radiations are projected onto the TE_{10} mode of the rectangular waveguide. Moreover, an excursion of the centroid is expected as the hyperfine amplitudes S_i undergo Rabi oscillations with respect to either the external electric field E_0 or the pulse duration τ. Such excursion was hinted in Ref. [22] to explain a $\sim$ 4 kHz line center discrepancy between measurements performed with two different experimental setups that may have used different MW pulse amplitude or duration.

In the remainder of this section, we assess the dependence of the line parameters to the amplitude E_0 for a fixed pulse duration τ = 175 ns. A similar experiment where τ is varied and E_0 is fixed is presented in Sec. B of the supplementary material. Fig. 6 displays the dynamics of the fitted line parameters with respect to the output amplitude of the digital-to-analog converter (DAC) of the DDS, expressed in % of the DAC vertical range. The output DAC amplitude is a proxy for E_0, since it is not directly measurable in our experiments. During this experiment, the output DAC amplitude was automatically incremented from 1% to 60% with a 1% step. The 60 resulting measured FIDs were fitted to retrieve the optimized line parameters. The top panel shows the estimated amplitudes of these FIDs. Even though the Rabi oscillations are clearly observed, the expression of Eq. 6 could not be fitted properly. The panel below shows the fit centroids and an excursion is clearly observed with respect to the excitation electric field E_0. To test whether this excursion was caused by the underlying hyperfine transitions, we measured the $R(0)$ transition of the hyperfine-free molecule OCS. A similar dynamic was observed for the fit line center, which invalidates the hypothesis where this effect would be linked to the HF structure. While the nature of this interesting effect remains unknown, the error caused by the Rabi line-shift is assessed by performing a linear fit of the estimated centroids shown in the inset of the panel. The difference between the intercept at zero excitation electric field and the centroid obtained at the $\pi/2$-pulse condition is -32 ± 10 Hz.

3.5. Long-term reproducibility

A total of three measurement campaigns were conducted for this project over a period of six months and are referred to hereafter in the chronological order as C1, C2 and C3. Only the results of the last campaign, i.e. C3, were presented in this work so far, but it is useful to consider C1 and C2 to assess the long-term reproducibility of the results. It must be mentioned that random instrumental modifications occurred between campaigns. For instance, the local oscillator was changed from a Keysight N5183B synthesizer used in C1 to an Anritsu 68067C synthesizer in C2. Also, the integrated-circuit of the PMA-183LN+ low noise amplifier was replaced from C2 to C3. Estimated line centers with respect to pressure for all measurement campaigns are displayed in Fig. 7. We define the long-term uncertainty as the largest difference $\Delta\nu_0$ for the centroid intercepts at zero pressure observed between all campaigns, that is $\Delta\nu_0$ = 117 Hz between C1 and C2. While the causes of these shifts remain unknown, they motivate the need for random hardware changes in the experimental setup to evaluate the untractable systematic effects.

3.6. Error budget

uncorrected ν_0	12 178 596 138	
	Δ_ν	σ_ν
Hyperfine	0	211
Rabi	-32	10
Post-processing	0	28
Frequency reference	0	< 1
Retesting	0	117
Sys. subtotal (Δ_ν^{sys} and σ_ν^{sys})	-32	243
Statistics	-	12
Total	**-32**	**243**
corrected ν_0	12 178 596 106	243

Table 1: Error budget for the centroid frequency ν_0 of the measured $2_0 \leftarrow 3_{-1}$ E transition in methanol. It includes the systematic and statistical contributions to ν_0, both in terms of correction Δ_ν and uncertainty σ_ν. All values in the table are reported in Hz.

A list of all systematic effects on the estimated centroid is provided in Table 1. The final centroid value for the 2_0 $E \leftarrow 3_{-1}$ E transition is the intercept at zero pressure determined in Sec. 3.3, corrected by the estimated shifts caused by the Rabi shift (Sec. 3.4). The final 1σ uncertainty level for the corrected centroid is the sum in quadrature of the systematics and statistical uncertainties identified in this work [49]. Finally, the last

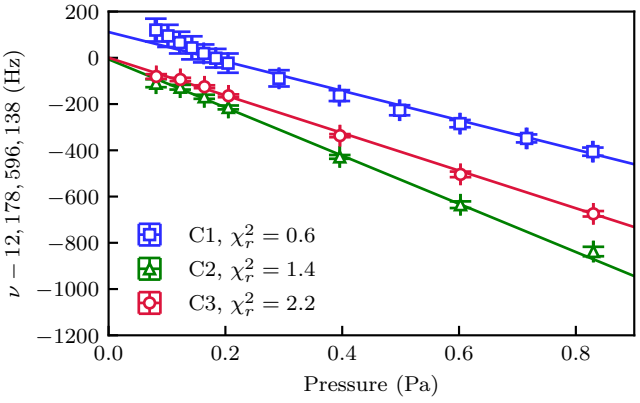

Figure 7: Average FID centroids estimated by fitting of the qSDV model to the three measurement campaigns C1, C2 and C3, as a function of pressure. Solid lines are the weighted linear least-squares fit of the different sets of estimated FID centroids.

contribution named "statistics" is defined as the largest centroid uncertainty σ_ν^{stat}, as plotted in Fig. 5 at $p \approx 0.6$ Pa. This value demonstrates the good reproducibility of the experiments conducted during the last measurement campaign, over a timescale of several days.

Table 2: Comparison of the line center of the $2_0\ E \leftarrow 3_{-1}\ E$ transition determined in this work compared to other references in the literature.

Reference	ν_0 (kHz)	$\Delta\nu$ (kHz)[a]	Method[b]
This work	12 178 596.1	0.2	WG
Gaines [19]	12 178 595	3	MA
Lovas [20]	12 178 593	8	BF
Breckendrige [21]	12 178 597	2	BF
Coudert [22]	12 178 600.2	0.8	BF

[a] Reported as 1σ standard uncertainty.
[b] Instrumental methods are waveguide spectrometer (WG), maser-beam spectrometer (MA) and Balle-Flygare instrument (BF).

The centroid frequency at zero pressure ν_0 of the $2_0\ E \leftarrow 3_{-1}\ E$ transition in methanol is reported at the end of the error budget. In Table 2, this value is compared with the line centers already published in the literature for the same transition. The centroid frequency obtained at the end of Table 1 is well within the 1σ uncertainties of the other works, except for the work of Coudert et al. in Ref. [22]. We identified two potential causes to explain this discrepancy. First, the authors reported for the center of the unweighted doublet they managed to resolve for the 12.2 GHz methanol line. This quantity may differ from the definition of the centroid we made in Eq. 1. Second, as discussed in Sec. 3.4, the use of specific parameters for the external microwave pulse may induce a Rabi line shift. In addition to the discrepancy discussed here, this effect may also explain the ~ 4 kHz deviation observed between the two independent measurements of the 12.2 GHz transition reported in Ref. [22].

4. Perspectives

The error budget presented in Sec. 3.6 compiles all the systematic effects that introduce additional uncertainty around the estimated centroid frequency ν_0. If all these were to be removed, then only the statistical uncertainty would remain. The latter corresponds to the largest centroid uncertainty σ_ν^{stat} observed in our experiments, that is $\sigma_\nu^{\text{stat}} = 12$ Hz at $p = 0.6$ Pa. In Fig. 8, we compare σ_ν^{stat} (black circles) to the Cramér-Rao lower bound for the FID frequency (dashed red line), denoted CRLB(ν), as a function of pressure. CRLB(ν) provides the smallest uncertainty achievable for the frequency estimation of a given FID signal, regardless of the estimation technique employed [50]. Based on Ref. [51], we derived the CRLB for the frequency estimate of a discrete Lorentzian FID signal (see Sec. C of the supplementary material). Following this development, CRLB(ν) may be expressed as:

$$\text{CRLB}(\nu) = \frac{6}{\pi^2} \frac{R(\Gamma_0)}{N \cdot \text{SNR}^2 \cdot T_{\text{FID}}^2} \tag{7}$$

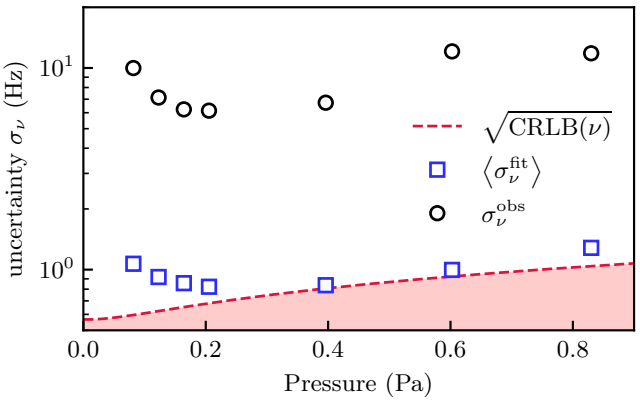

Figure 8: Statistical uncertainty σ_ν around the estimated centroid ν_0 with respect to methanol pressure. The black circles are the observed uncertainty σ_ν^{stat} defined as the standard deviation of the centroids estimated from the 34 fits per pressure setting (e.g., black vertical error bar in the inset of Fig. 5 for $p = 0.6$ Pa). $\langle\sigma_\nu^{\text{fit}}\rangle$ is the predicted fit uncertainty averaged over the 34 fits per pressure setting (e.g., blue error bars in in the inset of Fig. 5 for $p = 0.6$ Pa). The dashed red line is the square root of the theoretical Cramér-Rao lower bound for the variance of the FID frequency estimate. The red area indicates non-physical uncertainties as they would be located below $\sqrt{\text{CRLB}(\nu)}$.

This expression assumes an FID signal discretized in N samples, acquired over a time window of duration T_{FID}. Considering an additive white Gaussian noise of variance σ^2 and an FID of amplitude A, the SNR in Eq. 7 is defined as SNR $= A/\sigma$. The term $R(\Gamma_0)$ is an increasing function of the relaxation rate $\Gamma_0 \geq 0$ and evaluates to 1 for a constant FID envelope, i.e., $\Gamma_0 = 0$. The dashed red line in Fig. 8 is therefore the square root of Eq. 7, whose four parameters were fixed to their estimated experimental values. The non-zero slope of this curve comes from the fact that both SNR and Γ_0 depend on pressure. σ_ν^{stat} is about one order of magnitude larger than $\sqrt{\text{CRLB}(\nu)}$. However, $\langle\sigma_\nu^{\text{fit}}\rangle$, the fit uncertainty averaged over all 34 fits performed at a given pressure setting, closely matches $\sqrt{\text{CRLB}(\nu)}$ in the high-pressure range. $\langle\sigma_\nu^{\text{fit}}\rangle$ departs from $\sqrt{\text{CRLB}(\nu)}$ in the low-pressure range, where the Lorentzian assumption used to compute CRLB(ν) becomes less valid. The distinction between σ_ν^{stat} and $\langle\sigma_\nu^{\text{fit}}\rangle$ is stated in Sec. 3.3. In theory, these two quantities should coincide. Instead, a gap of one order of magnitude is observed and reflects the non-idealities of the measured FID signals which may be affected by non-stationary systematics. Therefore, if all systematic effects described above were fully managed, the frequency uncertainty would be limited by the statistical uncertainty, which in turn would be brought down to the CRLB limit. Uncertainties as low as $\sigma_\nu = 0.9$ Hz at $p = 0.4$ Pa could be achieved with the present experimental parameters. Perspectives for sub-Hz uncertainty ($\Delta\nu/\nu \sim 10^{-10}$) are therefore possible regarding the frequency estimation of microwave FIDs similar to the ones presented in this work. Such improvements will be explored in the near future.

5. Conclusions

Coherent microwave emission spectroscopy performed in a room-temperature waveguide cell offers an excellent control over many experimental parameters, not only in terms of sample pressure and temperature but also in terms of electromagnetic radiation, where the molecules are probed in the well-defined TE_{10} fundamental mode of the rectangular waveguide, in a background-free environment. It therefore provides a good platform to investigate the precision and accuracy that pertain to the line parameters. The present study focused on the centroid determination of the $2_0\ E \leftarrow 3_{-1}\ E$ CH_3OH line, motivated by its atmospheric, astrophysical and fundamental relevance. To this end, a time-domain line shape model that combines a quadratic speed-dependent Voigt profile and broad walls collisional relaxation was first selected to fit the experimental FIDs. Three systematic effects were estimated and corrected, with (i) the effect of the underlying hyperfine transitions, (ii), the pressure line-shift, (iii) the Rabi line-shift. The pressure line-shift was easily accounted for by extrapolating the estimated centroid frequencies to zero pressure. The resulting intercept is the initial value for ν_0 to which later corrections were applied. Even though the Rabi line-shift required a minimal -31 Hz correction in the default $\pi/2$-pulse conditions, it must be handled with care as it becomes large near integer multiples of π-pulse conditions. Long-term systematic effects with random hardware changes were also investigated and show that shifts as a large as ~ 117 Hz on the zero-pressure intercepts occur despite a day to day reproducibility as low as ~ 12 Hz. This observation stresses the importance of random hardware changes to evaluate the untractable systematics of the experiment. With all these effects taken into account, we provide a centroid frequency $\nu_0 = 12,178,596,106 \pm (12)_{\text{stat}} \pm (243)_{\text{sys}}$ Hz for the $2_0\ E \leftarrow 3_{-1}\ E$ transition in methanol. It represents a fractional uncertainty of $\Delta\nu/\nu = 2 \times 10^{-8}$. Finally, following the CRLB limit estimation, efforts to reduce these systematics are worthwhile since foreseeable fractional uncertainties as low as 10^{-10} with current FID parameters can be achieved (see Sec. C of the supplementary material).

Declaration of Competing Interest

The authors declare that they have no known competing financial interests or personal relationships that could have appeared to influence the work reported in this paper.

CRediT authorship contribution statement

Simon Collignon: Methodology, Investigation, Formal analysis, Visualization, Writing - original draft, Writing - review & editing. Brian Hays: Conceptualization, Methodology, Writing review & editing. Dimitri Lederer: Conceptualization, Funding acquisition, Methodology, Writing review & editing, Supervision. Clément Lauzin: Conceptualization, Funding acquisition, Methodology, Writing - original draft, Writing review & editing, Supervision.

Acknowledgment

The authors would like to thank François Rohart, Benoit Darquié, Mathieu Manceau and Boy Lankhaar for the useful discussions. The authors gratefully acknowledge the technical support of Marc Daman during the development of the spectrometer. The financial support of the FNRS through the "Mandat d'impulsion (MIS)" F.4038.24 and CDR J.0113.23, J.0124.26 and of the Fédération Wallonie-Bruxelles through the Action de Recherches Concertées (ARC, grant number ARC iBEAM-18/23-090) is gratefully acknowledged. The present research is part of the Space4ReLaunch project, which is supported by the SPW Economie Emploi Recherche of the Walloon Region, under the grant agreement nr 2210181.

References

[1] K. H. Bates, D. J. Jacob, S. Wang, R. S. Hornbrook, E. C. Apel, M. J. Kim, D. B. Millet, K. C. Wells, X. Chen, J. F. Brewer, E. A. Ray, R. Commane, G. S. Diskin, S. C. Wofsy, The Global Budget of Atmospheric Methanol: New Constraints on Secondary, Oceanic, and Terrestrial Sources, Journal of Geophysical Research: Atmospheres 126 (4) (2021) e2020JD033439. doi:10.1029/2020JD033439.
URL https://onlinelibrary.wiley.com/doi/abs/10.1029/2020JD033439

[2] W. Batrla, H. E. Matthews, K. M. Menten, C. M. Walmsley, Detection of strong methanol masers towards galactic H II regions, Nature 326 (6108) (1987) 49–51, publisher: Nature Publishing Group. doi:10.1038/326049a0.
URL https://www.nature.com/articles/326049a0

[3] K. M. Menten, The Discovery of a New, Very Strong, and Widespread Interstellar Methanol Maser Line, The Astrophysical Journal 380 (1991) L75. doi:10.1086/186177.
URL https://ui.adsabs.harvard.edu/abs/1991ApJ...380L..75M

[4] H. S. P. Müller, K. M. Menten, H. Mäder, Accurate rest frequencies of methanol maser and dark cloud lines, A&A 428 (3) (2004) 1019–1026. doi:10.1051/0004-6361:20041384.
URL https://www.aanda.org/articles/aa/abs/2004/48/aa1384/aa1384.html

[5] L. Błaszkiewicz, A. J. Kus, 12.2 GHz survey towards 6.7 GHz methanol masers - A comparison of 12.2 GHz and 6.7 GHz spectra, A&A 413 (1) (2004) 233–240, number: 1 Publisher: EDP Sciences. doi:10.1051/0004-6361:20031451.
URL https://www.aanda.org/articles/aa/abs/2004/01/aa3681/aa3681.html

[6] B. Lankhaar, W. Vlemmings, G. Surcis, H. J. van Langevelde, G. C. Groenenboom, A. van der Avoird, Characterization of methanol as a magnetic field tracer in

star-forming regions, Nat Astron 2 (2) (2018) 145–150, publisher: Nature Publishing Group. doi:10.1038/s41550-017-0341-8.
URL https://www.nature.com/articles/s41550-017-0341-8

[7] I. Kleiner, Spectroscopy of Interstellar Internal Rotors: An Important Tool for Investigating Interstellar Chemistry, ACS Earth Space Chem. 3 (9) (2019) 1812–1842, publisher: American Chemical Society.

[8] P. Jansen, L.-H. Xu, I. Kleiner, W. Ubachs, H. L. Bethlem, Methanol as a Sensitive Probe for Spatial and Temporal Variations of the Proton-to-Electron Mass Ratio, Phys. Rev. Lett. 106 (10) (2011) 100801, publisher: American Physical Society. doi:10.1103/PhysRevLett.106.100801.
URL https://link.aps.org/doi/10.1103/PhysRevLett.106.100801

[9] P. Jansen, I. Kleiner, L.-H. Xu, W. Ubachs, H. L. Bethlem, Sensitivity of transitions in internal rotor molecules to a possible variation of the proton-to-electron mass ratio, Phys. Rev. A 84 (6) (2011) 062505, publisher: American Physical Society. doi:10.1103/PhysRevA.84.062505.
URL https://link.aps.org/doi/10.1103/PhysRevA.84.062505

[10] S. A. Levshakov, M. G. Kozlov, D. Reimers, METHANOL AS A TRACER OF FUNDAMENTAL CONSTANTS, ApJ 738 (1) (2011) 26, publisher: The American Astronomical Society. doi:10.1088/0004-637X/738/1/26.
URL https://dx.doi.org/10.1088/0004-637X/738/1/26

[11] S. Muller, A. Beelen, M. Guélin, S. Aalto, J. H. Black, F. Combes, S. J. Curran, P. Theule, S. N. Longmore, Molecules at z = 0.89 - A 4-mm-rest-frame absorption-line survey toward PKS 1830−211, A&A 535 (2011) A103, publisher: EDP Sciences. doi:10.1051/0004-6361/201117096.
URL https://www.aanda.org/articles/aa/abs/2011/11/aa17096-11/aa17096-11.html

[12] S. P. Ellingsen, M. A. Voronkov, S. L. Breen, J. E. J. Lovell, FIRST COSMOLOGICAL CONSTRAINTS ON THE PROTON-TO-ELECTRON MASS RATIO FROM OBSERVATIONS OF ROTATIONAL TRANSITIONS OF METHANOL, ApJL 747 (1) (2012) L7, publisher: The American Astronomical Society. doi:10.1088/2041-8205/747/1/L7.
URL https://doi.org/10.1088/2041-8205/747/1/L7

[13] J. Bagdonaite, P. Jansen, C. Henkel, H. L. Bethlem, K. M. Menten, W. Ubachs, A stringent limit on a drifting proton-to-electron mass ratio from alcohol in the early universe, Science 339 (6115) (2013) 46–48.

[14] N. Kanekar, W. Ubachs, K. M. Menten, J. Bagdonaite, A. Brunthaler, C. Henkel, S. Muller, H. L. Bethlem, M. Daprà, Constraints on changes in the proton–electron mass ratio using methanol lines, Mon Not R Astron Soc Lett 448 (1) (2015) L104–L108. doi:10.1093/mnrasl/slu206.
URL https://doi.org/10.1093/mnrasl/slu206

[15] S. Muller, W. Ubachs, K. M. Menten, C. Henkel, N. Kanekar, A study of submillimeter methanol absorption toward PKS 1830−211: - Excitation, invariance of the proton-electron mass ratio, and systematics, A&A 652 (2021) A5, publisher: EDP Sciences. doi:10.1051/0004-6361/202140531.
URL https://www.aanda.org/articles/aa/abs/2021/08/aa40531-21/aa40531-21.html

[16] M. Safronova, D. Budker, D. DeMille, D. F. J. Kimball, A. Derevianko, C. W. Clark, Search for new physics with atoms and molecules, Rev. Mod. Phys. 90 (2) (2018) 025008, publisher: American Physical Society. doi:10.1103/RevModPhys.90.025008.
URL https://link.aps.org/doi/10.1103/RevModPhys.90.025008

[17] J.-P. Uzan, Fundamental constants: from measurement to the universe, a window on gravitation and cosmology, arXiv:2410.07281 [astro-ph] (May 2025). doi:10.48550/arXiv.2410.07281.
URL http://arxiv.org/abs/2410.07281

[18] R. M. Lees, F. J. Lovas, W. H. Kirchhoff, D. R. Johnson, Microwave Spectra of Molecules of Astrophysical Interest: III. Methanol, Journal of Physical and Chemical Reference Data 2 (2) (1973) 205–214. doi:10.1063/1.3253116.
URL https://doi.org/10.1063/1.3253116

[19] L. Gaines, K. H. Casleton, S. G. Kukolich, Beam Maser Measurements of CH_{3}OH Rotational Transitions, ApJ 191 (1974) L99. doi:10.1086/181559.
URL http://adsabs.harvard.edu/doi/10.1086/181559

[20] F. J. Lovas, R. D. Suenram, G. T. Fraser, C. W. Gillies, J. Zozom, The microwave spectrum of formamide–water and formamide–methanol complexes, J. Chem. Phys. 88 (2) (1988) 722–729. doi:10.1063/1.454151.
URL https://doi.org/10.1063/1.454151

[21] S. M. Breckenridge, S. G. Kukolich, Precise Laboratory Measurements of Methanol Rotational Transition Frequencies in the 5 to 13 GHz Region, The Astrophysical Journal 438 (1995) 504, publisher: IOP ADS Bibcode: 1995ApJ...438..504B. doi:10.1086/175095.
URL https://ui.adsabs.harvard.edu/abs/1995ApJ...438..504B

[22] L. Coudert, C. Gutlé, T. Huet, J.-U. Grabow, S. Levshakov, Spin-torsion effects in the hyperfine structure of methanol, The Journal of chemical physics 143 (4) (2015).

[23] P. Jansen, I. Kleiner, C. Meng, R. M. Lees, M. H. Janssen, W. Ubachs, H. L. Bethlem, Prospects for high-resolution microwave spectroscopy of methanol in a Stark-deflected molecular beam, Molecular Physics 111 (12-13) (2013) 1923–1930. doi:10.1080/00268976.2013.802819.
URL https://doi.org/10.1080/00268976.2013.802819

[24] F. Riehle, Frequency Standards: Basics and Applications, Wiley-VCH, 2004.

[25] S. L. Coy, Pressure dependence of rotational relaxation times T1 and T2 in the J=0−1 transition of OCS, J. Chem. Phys. 63 (12) (1975) 5145–5152. doi:10.1063/1.431296.
URL https://doi.org/10.1063/1.431296

[26] F. Rohart, H. Mäder, H. Nicolaisen, Speed dependence of rotational relaxation induced by foreign gas collisions: Studies on CH3F by millimeter wave coherent transients, J. Chem. Phys. 101 (8) (1994) 6475–6486. doi:10.1063/1.468342.
URL https://doi.org/10.1063/1.468342

[27] B. M. Hays, T. Guillaume, T. S. Hearne, I. R. Cooke, D. Gupta, O. Abdelkader Khedaoui, S. D. Le Picard, I. R. Sims, Design and performance of an E-band chirped pulse spectrometer for kinetics applications: OCS – He pressure broadening, Journal of Quantitative Spectroscopy and Radiative Transfer 250 (2020) 107001. doi:10.1016/j.jqsrt.2020.107001.
URL https://www.sciencedirect.com/science/article/pii/S0022407320300959

[28] L. Satterthwaite, G. Koumarianou, D. Sorensen, D. Patterson, Sub-hz differential rotational spectroscopy of enantiomers, Symmetry 14 (1) (2021) 28.

[29] D. W. Rein, Some remarks on parity violating effects of intramolecular interactions, J Mol Evol 4 (1) (1974) 15–22. doi:10.1007/BF01732768.
URL https://doi.org/10.1007/BF01732768

[30] C. Cohen-Tannoudji, J. DuPont-Roc, S. Haroche, F. Laloë, Detection of the Static Magnetic Field Produced by the Oriented Nuclei of Optically Pumped $^{3}\mathrm{He}$ Gas, Phys. Rev. Lett. 22 (15) (1969) 758–760, publisher: American Physical Society. doi:10.1103/PhysRevLett.22.758.
URL https://link.aps.org/doi/10.1103/PhysRevLett.22.758

[31] C. Gemmel, W. Heil, S. Karpuk, K. Lenz, C. Ludwig, Y. Sobolev, K. Tullney, M. Burghoff, W. Kilian, S. Knappe-Grüneberg, W. Müller, A. Schnabel, F. Seifert, L. Trahms, S. Baeßler, Ultra-sensitive magnetometry based on free precession of nuclear spins, Eur. Phys. J. D 57 (3) (2010) 303–320. doi:10.1140/epjd/e2010-00044-5.
URL https://doi.org/10.1140/epjd/e2010-00044-5

[32] R. Hong, S. Corrodi, S. Charity, S. Baeßler, J. Bono, T. Chupp, M. Fertl, D. Flay, A. García, J. George, K. L. Giovanetti, T. Gorringe, J. Grange, K. W. Hong, D. Kawall, B. Kiburg, B. Li, L. Li, R. Osofsky, D. Počanić, S. Ramachandran, M. Smith, H. E. Swanson, A. Tewsley-Booth, P. Winter, T. Yang, K. Zheng, Systematic and statistical uncertainties of the hilbert-transform based high-precision FID frequency extraction method, Journal of Magnetic Resonance 329 (2021) 107020. doi:10.1016/j.jmr.2021.107020.
URL https://www.sciencedirect.com/science/article/pii/S1090780721001099

[33] S. Kassi, C. Lauzin, J. Chaillot, A. Campargue, The (2–0) r (0) and r (1) transition frequencies of hd determined to a 10- 10 relative accuracy by doppler spectroscopy at 80 k, Physical Chemistry Chemical Physics 24 (38) (2022) 23164–23172.

[34] A. Altman, R. Tóbiás, A. S. Bogomolov, M. L. Diouf, F. M. J. Cozijn, A. G. Császár, C. Lauzin, W. Ubachs, Precise Frequencies of H216O Lines Protected for Radio Astronomy, ApJS 280 (2) (2025) 47, publisher: The American Astronomical Society. doi:10.3847/1538-4365/adfc68.
URL https://doi.org/10.3847/1538-4365/adfc68

[35] I. A. Finneran, D. B. Holland, P. B. Carroll, G. A. Blake, A direct digital synthesis chirped pulse Fourier transform microwave spectrometer, Review of Scientific Instruments 84 (8) (2013) 083104. doi:10.1063/1.4818137.
URL https://doi.org/10.1063/1.4818137

[36] L. Zou, R. A. Motiyenko, L. Margulès, E. A. Alekseev, Millimeter-wave emission spectrometer based on direct digital synthesis, Review of Scientific Instruments 91 (6) (Jun. 2020). doi:10.1063/5.0004461.
URL http://dx.doi.org/10.1063/5.0004461

[37] J. Chaillot, S. Dasari, H. Fleurbaey, M. Daeron, J. Savarino, S. Kassi, High-precision laser spectroscopy of H2S for simultaneous probing of multiple-sulfur isotopes, Environ. Sci.: Adv. 2 (1) (2023) 78–86, publisher: RSC. doi:10.1039/D2VA00104G.
URL https://pubs.rsc.org/en/content/articlelanding/2023/va/d2va00104g

[38] J. E. M. Heuvel, A. Dymanus, Hyperfine structure of CH3OH, Journal of Molecular Spectroscopy 45 (2) (1973) 282–292. doi:10.1016/0022-2852(73)90159-8.
URL https://www.sciencedirect.com/science/article/pii/0022285273901598

[39] B. Lankhaar, G. C. Groenenboom, A. van der Avoird, Hyperfine interactions and internal rotation in methanol 145 (24) (2016) 244301. doi:10.1063/1.4972004.
URL https://doi.org/10.1063/1.4972004

[40] H. Mäder, Microwave fourier transform spectroscopy: Linewidth effects in the low pressure limit, Journal of Quantitative Spectroscopy and Radiative Transfer 32 (2) (1984) 129–140. doi:10.1016/0022-4073(84)90077-3.
URL https://www.sciencedirect.com/science/article/pii/0022407384900773

[41] T. Köhler, , H. Mäder, Measurement of speed dependent rotational relaxation rates using a microwave spectrometer with a circular waveguide: Studies on nitrous oxide, Molecular Physics 86 (2) (1995) 287–300, publisher: Taylor & Francis. doi:10.1080/00268979500102021.
URL https://doi.org/10.1080/00268979500102021

[42] F. Rohart, A. Ellendt, F. Kaghat, H. Mäder, Self and Polar Foreign Gas Line Broadening and Frequency Shifting of CH3F: Effect of the Speed Dependence Observed by Millimeter-Wave Coherent Transients, Journal of Molecular Spectroscopy 185 (2) (1997) 222–233. doi:10.1006/jmsp.1997.7395.
URL https://www.sciencedirect.com/science/article/pii/S0022285297973951

[43] J. Tennyson, P. F. Bernath, A. Campargue, A. G. Császár, L. Daumont, R. R. Gamache, J. T. Hodges, D. Lisak, O. V. Naumenko, L. S. Rothman, H. Tran, N. F. Zobov, J. Buldyreva, C. D. Boone, M. D. D. Vizia, L. Gianfrani, J.-M. Hartmann, R. McPheat, D. Weidmann, J. Murray, N. H. Ngo, O. L. Polyansky, Recommended isolated-line profile for representing high-resolution spectroscopic transitions (IUPAC Technical Report), Pure and Applied Chemistry 86 (12) (2014) 1931–1943, publisher: De Gruyter. doi:10.1515/pac-2014-0208.
URL https://www.degruyterbrill.com/document/doi/10.1515/pac-2014-0208/html

[44] S. L. Coy, Speed dependence of microwave rotational relaxation rates, The Journal of Chemical Physics 73 (11) (1980) 5531–5555. doi:10.1063/1.440073.
URL https://doi.org/10.1063/1.440073

[45] L. Zou, R. A. Motiyenko, Window function for chirped pulse spectroscopy with enhanced signal-to-noise ratio and lineshape correction, Journal of Quantitative Spectroscopy and Radiative Transfer 268 (2021) 107608. doi:10.1016/j.jqsrt.2021.107608.
URL https://www.sciencedirect.com/science/article/pii/S0022407321001011

[46] D. W. Marquardt, An Algorithm for Least-Squares Estimation of Nonlinear Parameters, Journal of the Society for Industrial and Applied Mathematics 11 (2) (1963) 431–441, _eprint: https://doi.org/10.1137/0111030. doi:10.1137/0111030.
URL https://doi.org/10.1137/0111030

[47] P. Virtanen, R. Gommers, T. E. Oliphant, M. Haberland, T. Reddy, D. Cournapeau, E. Burovski, P. Peterson, W. Weckesser, J. Bright, S. J. van der Walt, M. Brett, J. Wilson, K. J. Millman, N. Mayorov, A. R. J. Nelson, E. Jones, R. Kern, E. Larson, C. J. Carey, i. Polat, Y. Feng, E. W. Moore, J. VanderPlas, D. Laxalde, J. Perktold, R. Cimrman, I. Henriksen, E. A. Quintero, C. R. Harris, A. M. Archibald, A. H. Ribeiro, F. Pedregosa, P. van Mulbregt, S. . Contributors, SciPy 1.0: Fundamental algorithms for scientific computing in python, Nature Methods 17 (2020) 261–272. doi:10.1038/s41592-019-0686-2.

[48] J.-U. Grabow, Fourier transform microwave spectroscopy measurement and instrumentation, in: Handbook of High-resolution Spectroscopy, John Wiley & Sons, Ltd, 2011. doi:10.1002/9780470749593.hrs037.
URL https://onlinelibrary.wiley.com/doi/abs/10.1002/9780470749593.hrs037

[49] BIPM, IEC, IFCC, ILAC, ISO, IUPAC, IUPAP, OIML, Evaluation of measurement data — Supplement 1 to the "Guide to the expression of uncertainty in measurement" — Propagation of distributions using a Monte Carlo method, Joint Committee for Guides in Metrology, JCGM 101:2008. doi:https://doi.org/10.59161/JCGM101-2008.

[50] S. M. Kay, Fundamentals of statistical signal processing: estimation theory, Prentice-Hall, Inc., USA, 1993.

[51] D. Hunter, M. S. Mrozowski, A. McWilliam, S. J. Ingleby, T. E. Dyer, P. F. Griffin, E. Riis, Optical pumping enhancement of a free-induction-decay magnetometer, J. Opt. Soc. Am. B, JOSAB 40 (10) (2023) 2664–2673, publisher: Optica Publishing Group. doi:10.1364/JOSAB.501086.
URL https://opg.optica.org/josab/abstract.cfm?uri=josab-40-10-2664